Earth and Planetary Science Letters 550 (2020) 116545

Contents lists available at ScienceDirect

Earth and Planetary Science Letters

www.elsevier.com/locate/epsl

Multicomponent diffusion of F, Cl and OH in apatite with application to magma ascent rates

Weiran Li [a,*], Sumit Chakraborty [b], Kazuhide Nagashima [c], Fidel Costa [a,d]

[a] Earth Observatory of Singapore, Nanyang Technological University, Singapore
[b] Ruhr Universität Bochum, Bochum, Germany
[c] HIGP, University of Hawai'i at Mānoa, Honolulu, HI, USA
[d] Asian School of Environment, Nanyang Technological University, Singapore

ARTICLE INFO

Article history:
Received 17 March 2020
Received in revised form 17 August 2020
Accepted 21 August 2020
Available online 3 September 2020
Editor: H. Handley

Keywords:
chemical zoning
igneous system
Merapi volcano
timescale
volatile

ABSTRACT

Chemical zoning in igneous minerals is a potential record of the time, processes, and thermal evolution during the lifetime of a given magma reservoir. Abundances of volatiles (OH, Cl and F) in apatite from terrestrial and extraterrestrial plutonic and volcanic rocks have been used to study volatile behavior in magmas, however, volatile diffusivities in apatite are poorly constrained. Here we report new experimental results on Cl, F and OH diffusivities in apatite and apply them to estimate magma ascent times and rates. The experiments were carried out on oriented natural Durango fluorapatite crystals at 800–1100 °C, 1-atm, and oxygen fugacity at the wüstite-magnetite buffer. Experimental charges and chemical profiles were investigated with a variety of methods, including scanning electron microscopy, transmission electron microscopy, electron probe microanalysis, secondary ion mass spectrometry, and nuclear reaction analysis.

We find that the concentration profiles of Cl show evidence of uphill diffusion that is likely related to the co-existence of three monovalent anions, i.e., OH^-, Cl^-, F^-, at the same site of the apatite structure. Chemical gradients of OH, Cl and F were reproduced using a multicomponent diffusion model to extract the tracer diffusion coefficient (D_i^*) of each component (i). The calculated values of D_i^* parallel to the ***c***-axis show a general relation of $D_F^* > D_{Cl}^* > D_{OH}^*$, and define the following Arrhenius relations (parallel to the ***c***-axis, at 1 bar) as:

$$D_{Cl}^* = 7\begin{pmatrix}+12\\-4\end{pmatrix} \times 10^{-5} \times \left[exp\left(\frac{-294\,(\pm 12)\ \text{kJ}\cdot\text{mol}^{-1}}{RT} \right) \right] \text{m}^2\cdot\text{s}^{-1}$$

$$D_F^* = 5\begin{pmatrix}+49\\-5\end{pmatrix} \times 10^{-4} \times \left[exp\left(\frac{-308\,(\pm 76)\ \text{kJ}\cdot\text{mol}^{-1}}{RT} \right) \right] \text{m}^2\cdot\text{s}^{-1}$$

$$D_{OH}^* = 4\begin{pmatrix}+11\\-3\end{pmatrix} \times 10^{-2} \times \left[exp\left(\frac{-401\,(\pm 39)\ \text{kJ}\cdot\text{mol}^{-1}}{RT} \right) \right] \text{m}^2\cdot\text{s}^{-1}$$

The activation energy for Cl diffusion that we determined (294 $\text{kJ}\cdot\text{mol}^{-1}$) is within the range of that reported by Brenan (1994), but the pre-exponential factor is smaller and thus we obtain in general slower diffusivities than Brenan (1994). D_{Cl}^* and D_{OH}^* parallel to the ***a***-axis are 1 to 2 orders of magnitude slower than those parallel to the ***c***-axis, indicating anisotropic diffusion of Cl and OH. Preliminary results on S diffusivity (parallel to the ***c***-axis) at 800–900 °C show values between those of Cl and OH. The diffusion coefficients and model proposed in this study can be used to estimate the timescales of volatile re-equilibration in apatite in a variety of contexts from plutonic rocks and layered intrusions, to volcanic rocks and meteorites. We show that, for example, magma ascent rates can be determined by modelling Cl zoning in volcanic apatite. These applications provide new opportunities for understanding the influence of magma ascent rates on the eruption styles of volcanoes, thus having potential contributions to improving volcano forecasting and hazard assessments.

* Corresponding author.
E-mail address: weiran.li@ntu.edu.sg (W. Li).

https://doi.org/10.1016/j.epsl.2020.116545
0012-821X/

1. Introduction

Apatite is a common mineral in terrestrial igneous, metamorphic, and sedimentary rocks (Piccoli and Candela, 1994; Boudreau, 1995; Peng et al., 1997; Boyce and Hervig, 2008, 2009; Van Hoose et al., 2013; Kusebauch et al., 2015; Scott et al., 2015; Webster and Piccoli, 2015; Stock et al., 2018), in lunar rocks (McCubbin et al., 2010; Greenwood et al., 2011; Boyce et al., 2014; Ustunisik et al., 2015; Brounce et al., 2019; Wang et al., 2019), and from Martian meteorites (Greenwood et al., 2008; McCubbin and Nekvasil, 2008). Apatite can incorporate various volatile species (e.g. fluorine, chlorine, hydroxyl, oxygen, sulfur, carbonate) into its crystallographic structure (Piccoli and Candela, 2002; Hughes and Rakovan, 2015), and has been used to estimate magmatic volatile budgets based on the apatite-melt volatile partitioning (e.g. Li and Costa, 2020). However, it is important to evaluate whether the volatile records in apatite have been modified via diffusion by changing temperature, pressure and volatiles contents during the lifetime of the crystal. Evidence of partial re-equilibration of apatite has been observed from the zoning of chlorine (Cl) and hydroxyl (OH) at the crystal rims of volcanic apatite (from $<$80 μm to $>$300 μm in length; Boyce and Hervig, 2008; Scott et al., 2015) and plutonic apatite (Cornejo and Mahood, 1997). Evaluating the extent of diffusion-induced re-equilibration of apatite requires the knowledge of F, Cl and OH diffusivities.

A few experimental studies have been conducted on the diffusivities of cations (e.g. Sr, Pb, U, Th, REEs; Cherniak, 2010) and noble gas elements (e.g. He; Baxter, 2010), but only one study has determined the diffusivities of F and Cl (Brenan, 1994). Brenan (1994) found that Cl diffusion in apatite is anisotropic, i.e., faster parallel to the $\boldsymbol{c}$-axis ($\parallel \boldsymbol{c}$) than parallel to the $\boldsymbol{a}$-axis ($\parallel \boldsymbol{a}$), which is related to a faster Cl migration within the anion column parallel to the $\boldsymbol{c}$-axis of the apatite structure (Piccoli and Candela, 2002; Hughes and Rakovan, 2015), and is able to explain the anisotropic Cl zoning observed from natural crystals (Boyce and Hervig, 2008). Brenan (1994) also found that at a single temperature, Cl diffusivities $\parallel \boldsymbol{c}$ show a 6-fold variation depending on the OH abundances in the crystals, implying a compositional effect that needs more experimental investigation. In addition, natural apatite is commonly zoned of sulfur (S) (Van Hoose et al., 2013; Scott et al., 2015; Li, 2019) and has been used to study S contents of magmas, but S diffusivity in apatite has not been determined.

We performed experiments to determine the diffusivities of Cl, F, OH and S in apatite at 800–1100 °C, 1-atm, and oxygen fugacity at the wüstite-magnetite buffer. Experimental charges were analyzed using a variety of techniques to acquire diffusion profiles, and the measured profiles were used to determine diffusion rates using a multicomponent diffusion model that considers the coupling between fluxes of F, Cl, and OH. The new diffusion coefficients were used to calculate timescales of F-Cl-OH diffusion in natural crystals emitted from an effusive (dome-forming) and explosive eruptions at Merapi volcano (Indonesia), and the pre-eruptive magma ascent rates. The new diffusion data and model proposed in this study provide a new tool for investigating the time-rates of magma ascent and their influences on the eruptive styles of volcanoes.

2. Experimental and analytical approaches

2.1. Starting materials and two types of diffusion couples

Starting materials were gem-quality natural apatite crystals from Durango (Mexico), and Morocco (purchased from Excalibur Mineral Corp, USA). Their volatile compositions were determined using a Cameca ims-1280 secondary ion mass spectrometer at the University of Hawai'i at Mānoa, USA, and show distinct concentrations of F, Cl, H_2O and S (Supplementary Table S1). Given that H_2O occurs as OH in apatite (e.g. Piccoli and Candela, 2002), the determined concentrations of H_2O were converted into OH (based on 1 mole H_2O = 2 moles OH). The Durango apatite is compositionally similar to the endmember fluorapatite (mole fraction: $X_F \approx 92\%$, $X_{Cl} \approx 5\%$, $X_{OH} \approx 3\%$) and contains ~1600 ppm S, whereas the Morocco apatite is poorer in F (~2.8 wt.%) and S ($\leq$15 ppm), but richer in Cl and OH (mole fraction: $X_F \approx 66\%$, $X_{Cl} \approx 11\%$, $X_{OH} \approx 23\%$). The Durango apatite analyzed using an electron microprobe also shows similar F-Cl contents with variation of $<$0.1 wt.% from the rim to core of the crystal (Supplementary Table S1; Fig. 4). Both starting crystals are poor in CO_2 ($<$34 ppm), thus CO_2 has negligible effect on our results.

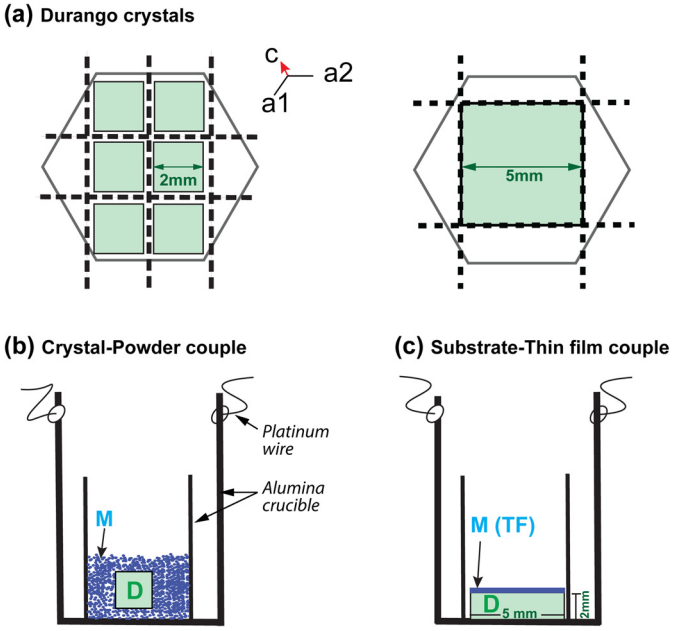

Fig. 1. (a) Durango apatite crystals cut into small cubes ($2 \times 2 \times 2$ mm^3) or cuboids ($5 \times 5 \times 2$ mm^3), shown in a view parallel to the $\boldsymbol{c}$-axis. (b) A diffusion couple made up of a F-rich Durango cube (D) with its polished side facing downward, embedded in powders made from Cl- and OH-rich Morocco apatite crystals (M). (c) A Diffusion couple made up of a Durango cuboid (D) and a laser deposited thin film (TF) made from Morocco apatite powders.

The two types of starting crystals were used to make the diffusion couples. The Morocco crystals were ground into fine powders ($<$100 μm in length) using an agate mortar, and the Durango crystals (oriented either parallel or normal to their $\boldsymbol{c}$-axes) were cut into 2-mm-thick slices using a wire saw. Orientations of the Durango crystals were analyzed *a posteriori* using electron backscatter diffraction technique (EBSD), showing $<3°$ tilts from the expected orientations. The cut slices were mounted in epoxy and polished using diamond compounds (from 3 μm to 0.25 μm), and a highly alkaline colloidal silica solution (OPS). The polished slices were cut into cuboids ($5 \times 5 \times 2$ mm^3), or cubes ($2 \times 2 \times 2$ mm^3) to make diffusion couples in two forms: Type-1 consists of a Durango apatite cube embedded in Morocco apatite powders (referred to as crystal-powder couple), and Type-2 consists of a Durango apatite cuboid deposited with a thin film made from the Morocco apatite (referred to as substrate-thin film couple). Thin films were deposited using the pulsed laser deposition technique (PLD; cf.

Dohmen et al., 2002), where a pellet (compressed from powders of Morocco apatite) was ablated by a 10-Hz pulsed laser for a few minutes. The laser power and durations used for depositions are: 212 mJ, 15 mins for sample *DAp7* (sample label marked in italic hereafter); 192 mJ, 5 mins for *DAp9* and *DAp11*; and 96 mJ, 7 mins for *DAp15* and *DAp16*. According to the birefringence color of thin films and refractive indices of apatite (≈1.63), the thickness of thin films was estimated to be ~100–200 nm (see the texture and composition of thin films in Section 3.2).

Diffusion couples were placed in small alumina crucibles (~8 mm in diameter). For the crystal-powder couples, the polished sides of the crystals were placed facing the bottom of the crucible for good contact with the powders (Fig. 1a), whereas for the substrate-thin film couples, the samples were placed with the thin film facing upward (Fig. 1b). The alumina crucible was placed in a larger alumina crucible (~2 cm in diameter), and tied to an alumina rod (with platinum wires) before loaded into the furnace (Fig. 1c). All crucibles have opening on top such that the samples were exposed to the furnace atmosphere during experiments.

2.2. Experimental conditions

Diffusion anneals were performed in a vertical gas-mixing furnace at atmospheric pressure. Temperatures were monitored with a B-type thermocouple placed within 2 cm away from the sample container and remained within ±2 °C of the desired temperature during experiments. Oxygen fugacity (fO_2) was maintained at the wüstite-magnetite (WM) buffer (e.g. $fO_2 = 5.0 \times 10^{-12}$ bars, at 1100 °C), using a continuous CO-CO_2 gas flow. The furnace was equilibrated to the run conditions (i.e., the desired T and fO_2) for >30 mins, after which the crystals were loaded into the furnace close to the thermocouple. For investigation of diffusion $\| \boldsymbol{c}$, four crystal-powder couples were run at 1100 °C for about 17, 66, and 161 hours, and four substrate-thin film couples were run at 800–1000 °C for ~40–220 minutes (Table 1). Another substrate-thin film couple was run at 950 °C for ~21 hours for investigation of diffusion $\| \boldsymbol{a}$. Experiments were terminated by quickly removing the samples from the furnace for annealing into air, where the temperatures quickly dropped down to <100 °C within 2–3 minutes.

2.3. EPMA analysis of the crystal-powder couples

Annealed crystals 3d, 6*d*#1 and #2 were taken out of their surrounding powders, and mounted in epoxy with their polished sides placed perpendicular to the epoxy surface. To investigate the interface between the crystal and powders, one crystal (*4d*) was kept within the powders, consolidated using epoxy, and sectioned together with the alumina crucible (Supplementary Fig. S9).

X-ray maps and compositional profiles were acquired for unannealed and annealed crystals, using a JEOL JXA 8530F field emission gun electron microprobe. To investigate volatile distribution at different directions, X-ray maps of F, Cl and S (~100 × 100 μm^2 in size) were acquired from the corner of each crystal, using an accelerating voltage of 15 kV, beam current of 25 nA, and dwell time of ~70 ms. Compositional profiles with 1-μm spacing were acquired from the middle of the polished face towards the crystal core (perpendicular to crystal boundary), using a voltage of 15 kV and a focused beam with low current (10 nA) to minimize F migration during analysis. The effect of F migration during EPMA analysis is negligible, considering that all crystals were mounted with their ***c***-axes perpendicular to the electron beam (Stormer et al., 1993; Stock et al., 2015). Standards used for analysis and the data corrections are the same as reported in Li (2019), where a long on-peak counting time (~120 s) was used for acquiring high-precision measurement of Cl. H_2O concentrations determined by EPMA were

Table 1
Summary of experimental conditions (1-atm, wüstite-magnetite buffer), and calculated diffusivities of F, Cl, OH and S.

	Orientation	T (°C)	Time (hrs)	log fO_2	D_F^* (m^2/s)		D_{Cl}^* (m^2/s)		D_{OH}^* (m^2/s)		D_S (m^2/s)
					Best fit	Range	Best fit	Range	Best fit	Range	Best fit
Crystal-powder couples											
3d	$\| c$	1101	17	−11.30	1×10^{-15}	1×10^{-16}–1×10^{-14}	4×10^{-16}	(2–6) × 10^{-16}	2×10^{-17}	1×10^{-17}–5×10^{-16}	n.a.
4d	$\| c$	1104	66	−11.30	1×10^{-15}	1×10^{-16}–1×10^{-14}	4×10^{-16}	(3–5) × 10^{-16}	2×10^{-17}	1×10^{-17}–4×10^{-17}	n.a.
6d#1	$\| c$	1100	161	−11.02	1×10^{-15}	6×10^{-16}–1×10^{-14}	5×10^{-16}	(3–8) × 10^{-16}	2×10^{-17}	1×10^{-17}–5×10^{-17}	n.a.
6d#2	$\| c$	1100	161	−11.02							
Substrate-thin film couples											
DAp9 [1]*	$\| c$	804	3.67	−15.44	n.a.	n.a.	4×10^{-19}	(3–6) × 10^{-19}	n.a.	n.a.	1.2 (± 0.8) × 10^{-19}
DAp11#1 [1]	$\| c$	900	0.67	−14.78	1×10^{-17}	8×10^{-19}–1×10^{-16}	8×10^{-18}	(6–10) × 10^{-18}	5×10^{-20}	1×10^{-21}–1×10^{-19}	1.5 (± 0.7) × 10^{-18}
DAp15 [2]	$\| c$	900	2.00	−14.76	1×10^{-17}	8×10^{-19}–1×10^{-16}	3×10^{-18}	(2–3) × 10^{-18}	5×10^{-20}	1×10^{-20}–1×10^{-19}	1.2 (± 0.7) × 10^{-18}
DAp7 [3]	$\| c$	998	2.00	−12.64	n.a.	n.a.	7×10^{-17}	(4–10) × 10^{-17}	n.a.	n.a.	n.a.
DAp16 [2]	$\| a$	950	21.12	−13.57	2×10^{-18}	1×10^{-19}–5×10^{-17}	1.2×10^{-19}	(1–2) × 10^{-19}	6×10^{-21}	2×10^{-21}–2×10^{-20}	3.0 (± 0.5) × 10^{-20}

* Numbers in brackets indicate thin films that were deposited using different laser power for different durations: [1] *TF4*; [2] *TF7*; [3] *TF2*.

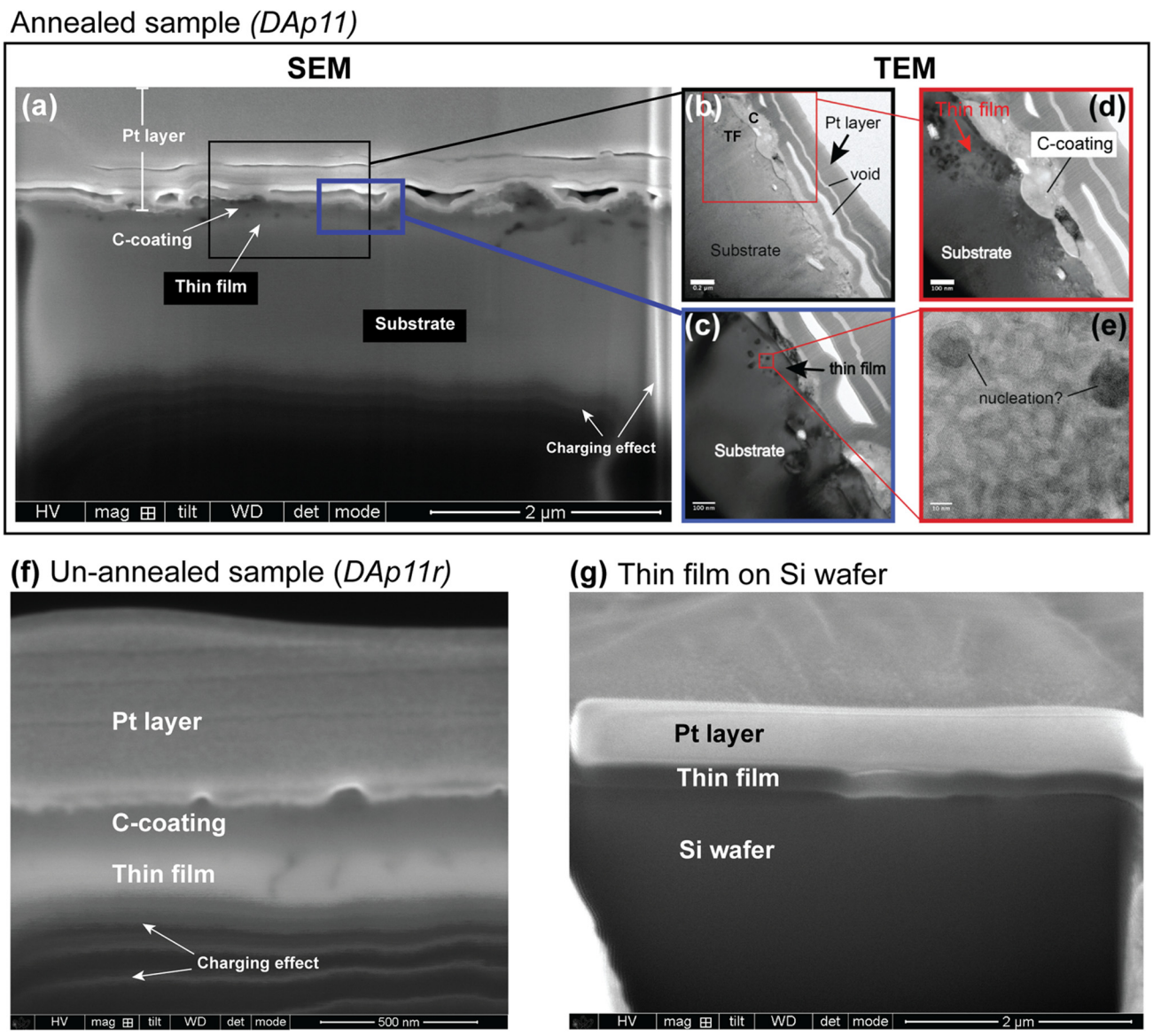

Fig. 2. Cross section of a thin film-substrate (apatite) sample (*DAp11*, annealed at 900 °C for 0.67 hours) shown in SEM (panel *a*) and TEM bright-field images (panel *b-e*); and cross sections of un-annealed thin films on apatite substrate (*DAp11r*, panel *f*), and on silicon wafer (panel *g*), shown in SEM images. The thin film of *DAp11* is about 100- to 200-nm thick and shows some heterogeneous structures with perhaps a few nuclei (panels *c-e*) formed by re-crystallization during/after the annealing. The unannealed thin films seem to be more homogeneous. Voids between the several platinum layers above the thin film of *DAp11* (dark areas in panel *a*, and bright areas in panels *b-d*) are artifacts produced by multiple-time deposition of Pt on this sample, before it was sectioned using FIB for the TEM observation (see text). Scale bars are 200 nm in panel *b*, 100 nm in panels *c-d*, and 10 nm in panel *e*.

calculated assuming apatite stoichiometry (cf. Ketcham, 2015). Relative errors in the determined concentrations are <1% for the major elements in apatite (e.g. Ca, P), ~1.5% for F, ~1% for Cl, and ~7–10 % for S.

2.4. TEM, SIMS, AFM and NRA analyses of the substrate-thin film couples

To investigate the interface between substrates and thin films, we cut thin foils perpendicular to the surface of two samples whose thin films were deposited simultaneously (*DAp11* – annealed; *DAp11r* – unannealed), and observed them using a transmission electron microscope (TEM) (see Supplementary material). Both samples show good contact between thin film and substrate (Fig. 2).

Depth profiles of OH, F, Cl, S, and P were acquired from five annealed and two unannealed samples, using a Cameca ims-1280 secondary ion mass spectrometer (SIMS) at University of Hawai'i at Mānoa (USA). The samples were coated with gold of ~30 nm in thickness, and loaded in SIMS airlock sample chamber for >20 hours before analysis. Using LN_2 trap, the sample chamber was kept under $<10^{-9}$ torr during all analyses. The central area of each sample was analyzed using a primary Cs^+ beam accelerated to 10 keV and adjusted to ~600 pA, with spot size of ~5 µm. Secondary ions of $^{16}OH^-$, $^{18}O^-$, $^{31}P^-$, $^{34}S^-$, $^{19}F^{16}O^-$, $^{37}Cl^-$ were collected using an electron multiplier. The mass resolving power (MRP: ~6000) is high enough to separate the targeted ions from the interferential ones. After about 2–3 minutes pre-sputtering, scanning ion images (SIIs) were obtained for in total 180–350 cycles over $\sim 50 \times 50$ µm^2 raster areas. Some SIIs show heterogeneous distribution of $^{16}OH^-$ and $^{37}Cl^-$, and to minimize their effects on the calculated diffusivities, we selected the nearly homogeneous areas (~40–70 µm^2) at the center of the SIIs to reconstruct depth profiles (Supplementary Figs. S1-S4).

Profile lengths were determined by measuring depths of individual SIMS pits using Atomic Force Microscopy (AFM) (Supple-

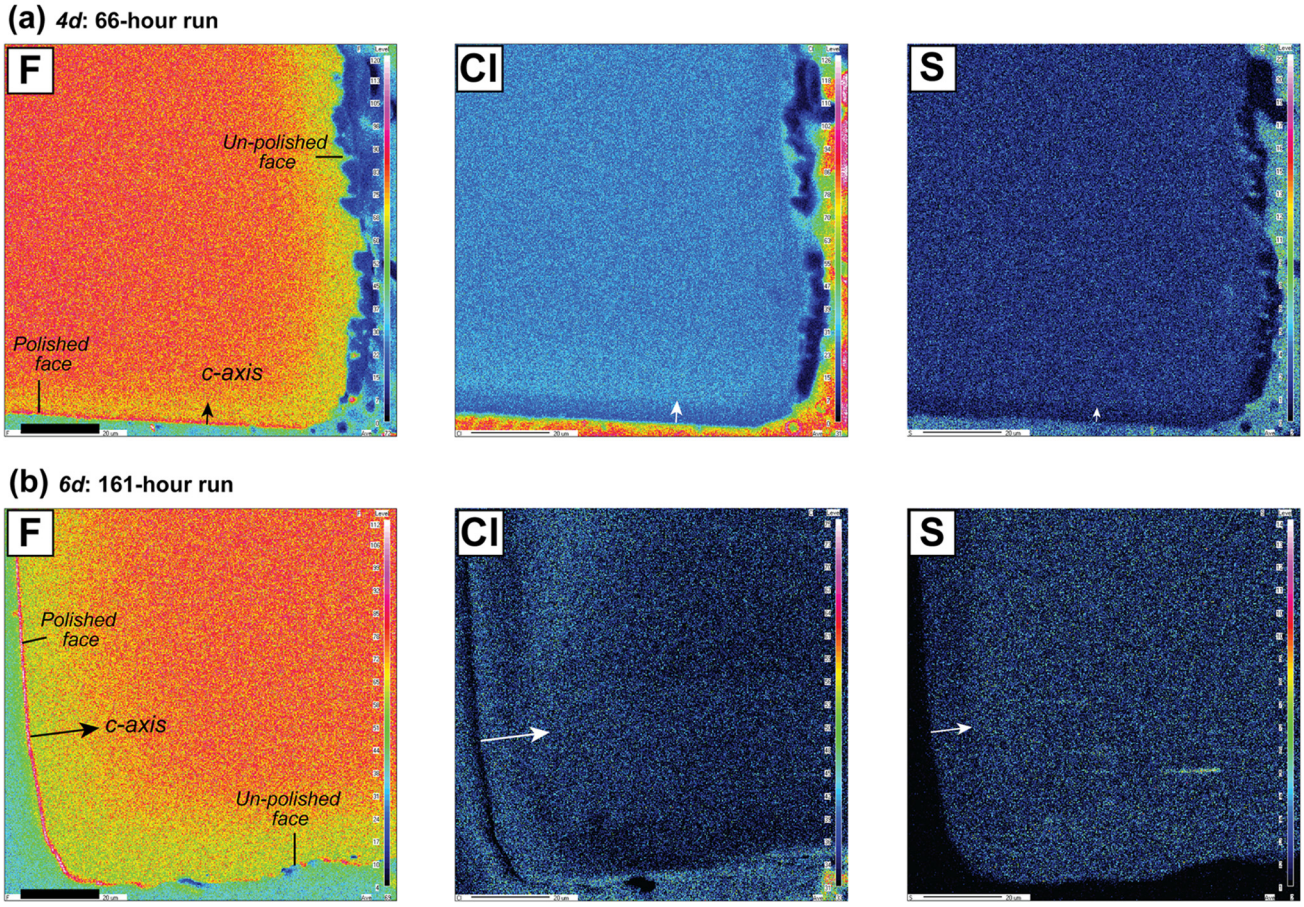

Fig. 3. Compositional distribution of F, Cl, and S in two crystals annealed at 1100 °C for 66 hours (sample 4*d* in panel *a*), and 161 hours (sample 6*d*#1 in panel *b*). The directions of arrows show the ***c***-axis perpendicular to the polished face of the crystal, and their lengths show diffusion distances. Scale bars are 20 μm. (For interpretation of the colors in the figure(s), the reader is referred to the web version of this article.)

mentary Fig. S5). Nuclear reaction analysis (NRA) was also used to acquire F profiles for comparison with those measured by SIMS (Supplementary Fig. S8).

3. Observation of run products

3.1. Crystal-powder couples

The annealed crystals observed using optical microscope and SEM show smooth boundary of the polished faces at crystal rims with no sign of re-crystallization (Supplementary Fig. S9). Based on this, the powders that surround the crystals have been treated as an effective infinite diffusion source with constant composition of the concerned components during experiments. This is also supported by the similar F-Cl-OH composition between the powders near the interface and the crystal rim (by EPMA; Supplementary Fig. S10).

3.2. Substrate-thin film couples

Thin foils cut perpendicular to the surface of unannealed and annealed samples were observed using SEM and TEM. The thin film and substrate show good contact at the interface and similar greyscales in backscattered images acquired with SEM (Fig. 2a). TEM images that have higher spatial resolution show that the annealed thin film is less homogeneous (than the substrate) and contains some nuclei (~10–50 nm in size) (Fig. 2b-e). Such nuclei were not seen in un-annealed thin films (Fig. 2f, g), implying that the originally amorphous thin film had some extent of re-crystallization during annealing. This can also explain why the annealed thin films are more heterogeneous than the unannealed ones, as were seen in the secondary ion images by SIMS (Supplementary Figs. S1-4).

4. Measured diffusion profiles

Given the different length scales of diffusion in the two types of diffusion couples (i.e., in nanometers and micrometers), we have acquired diffusion profiles from the crystal-powder couples using EPMA, and those of the substrate-thin film couples using SIMS and NRA.

4.1. Concentration profiles of crystal-powder couples

X-ray maps of F from 6*d*#1 and 4*d* run products annealed at 1100 °C for different durations show a similar zoning pattern, i.e., decreasing F intensities towards the crystal rim, over similar distances parallel and normal to the crystal ***c***-axis (Fig. 3). Cl zoning shows a more complex pattern over longer distances parallel to the crystal ***c***-axis than normal to it. The S concentrations decrease towards the crystal rims over shorter distances than F and Cl.

Concentration profiles by EPMA show decreasing F and increasing H_2O towards the crystal rim (Fig. 4), where diffusion profiles in 6*d*#1 and #2 run products (annealed for 161 hours) are about twice longer than those in 4*d* (annealed for 66 hours). Cl profiles of three crystals (4*d*, 6*d*#1 and 6*d*#2) show high-Cl peaks away from their rims (Fig. 4b), reflecting the so-called uphill diffusion (see below), and the high-Cl peaks found in 6*d*#1 and #2 appear

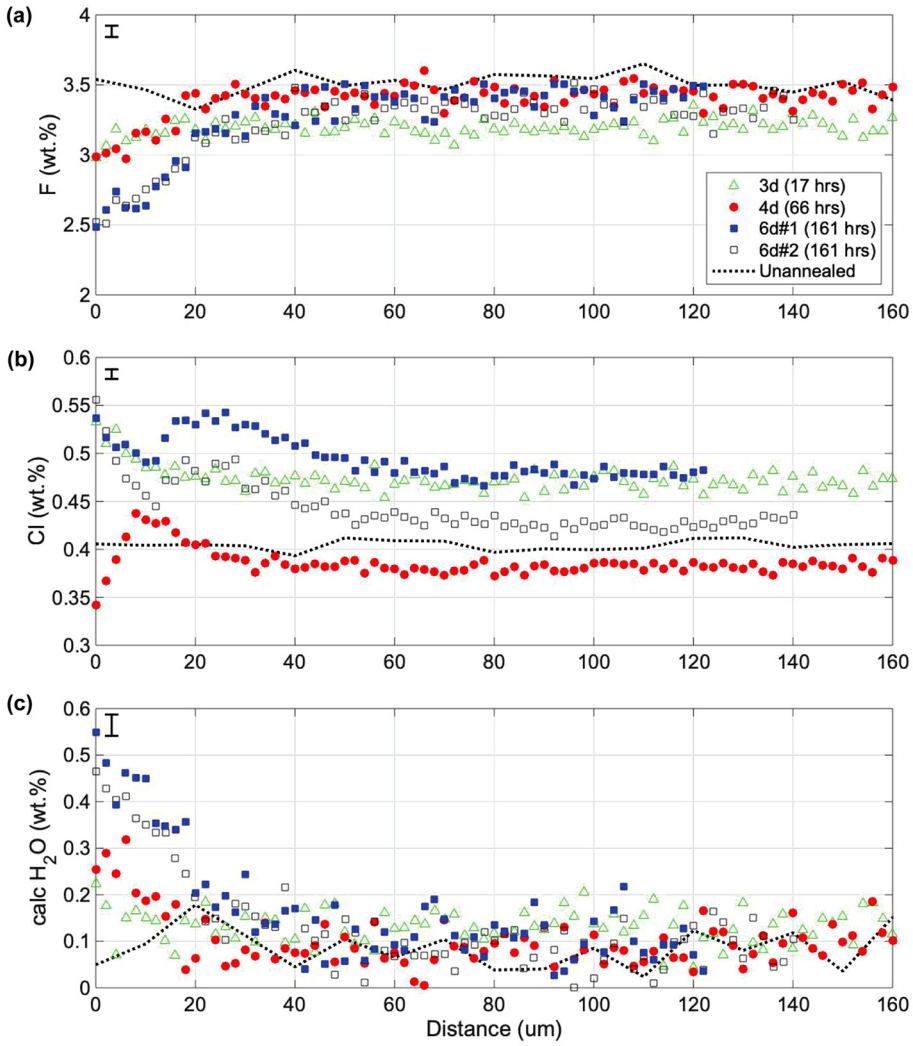

Fig. 4. Concentration profiles of F, Cl (both measured using EPMA) and H_2O (calculated from stoichiometry), obtained parallel to the ***c***-axis of an unannealed crystal, and four other crystals that were annealed at 1100 °C for different durations (3*d*: ~17 hours, 4*d*: ~66 hours, 6*d*#1 and #2 from the same run of ~161 hours). The Cl profiles of 4*d*, 6*d*#1 and 6*d*#2 show uphill diffusion. Concentrations at the boundary of the two crystals from the same run (6*d*#1, #2) are similar, but different from those of the other two samples, reflecting different compositions of the powders in contact with the crystal rims. Compositional variations in unannealed crystal (reflecting heterogeneity of starting Durango apatite) are much smaller than those caused by diffusion in annealed crystals. Error bars show 2 s.d. of F and Cl concentrations measured using EPMA, and H_2O calculated from stoichiometry.

further away from the crystal rims (over distances of ~20–30 μm) than that found in 4*d* (over a distance of ~8–10 μm).

The unzoned areas of annealed crystals show different F-Cl-H_2O compositions from the unannealed crystals (Fig. 4), reflecting some extent of compositional heterogeneity of the starting crystals. Considering this, we have used the compositions measured from the unzoned areas of each crystal as the initial condition in diffusion modelling. It is worth noting that the compositional variation within the unzoned areas of individual crystals is much smaller than the diffusion-induced compositional change near/at the crystal rim.

The crystal rim of 4*d* and the powders next to it have similar F-H_2O concentrations, but higher Cl in powders, i.e., approximately equal to the highest Cl content of the crystal (at the "uphill" peak) (Supplementary Fig. S10). Compared to the unannealed Morocco apatite, annealed powders show similar F-H_2O concentrations, but less Cl (of ~0.2 wt.%). Such depletion of Cl was also observed in un-annealed thin films that were made from the same batch of powders, indicating its cause by the heterogeneity of Cl contents of the starting Morocco apatite, rather than a Cl loss during experiments. Considering this, we have used the F-Cl-OH composition measured from each crystal rim as the boundary condition in diffusion modelling.

4.2. Depth profiles of substrate-thin film couples

Secondary ion intensities of F, Cl, OH and S (by SIMS) were converted into concentrations using calibration curves determined from SIMS analysis of un-annealed Durango fluorapatite (see compositions in Supplementary Table S1). Total lengths of depth profiles were determined using AFM (see the Supplementary Material).

4.2.1. Un-annealed sample

The thin film of unannealed sample *DAp3r* is lower in F, but higher in Cl and OH than the substrate (Supplementary Fig. S7), which is expected according to the compositions of the two starting crystals. P intensities in the thin film are only about half of those in the substrate (Supplementary Fig. S7e), implying different structures between the thin film and substrate. The transition in P signals between the two phases occurs over a distance of ~20 nm, reflecting combined influences of surface mixing by the sputtering of SIMS, and the topography of thin film (with roughness

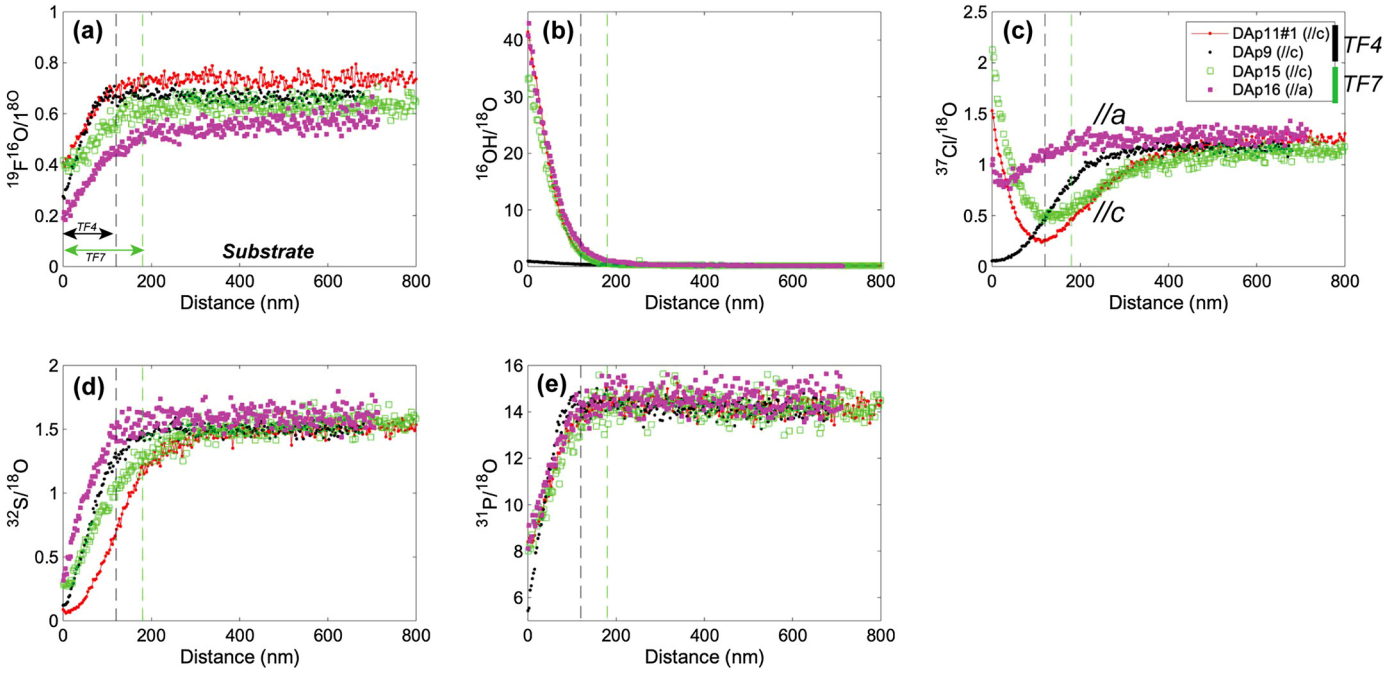

Fig. 5. Depth profiles of (a) F, (b) OH, (c) Cl, (d) S and (e) P measured parallel to the ***c***-axes ($\parallel$ ***c***) of three annealed thin-film samples, and parallel to the ***a***-axis ($\parallel$ ***a***) of one sample (see legend), using SIMS. Vertical dashed lines were determined from the kink points of P profiles (panel *e*), which reflect the approximate locations of the interface between thin film and substrate (without counting the mixing layers at the interface; see text). Thin films produced by pulsed laser deposition for a longer duration have larger thickness (*TF7*: ~170 ± 10 nm) than those deposited for a shorter duration (*TF4*: ~120 ±10 nm).

of ~9 nm determined by AFM; Supplementary Fig. S6). Compared to P, the thickness of mixing layers of other ions are larger, i.e., ~30 nm for OH^-, ~35 nm for F^-, and ~50 nm for Cl^-, but still much smaller than the diffusion penetration lengths (~400–800 nm for Cl; ~100–400 nm for F, OH). Therefore, the resultant overestimation of the calculated diffusivities (cf. Ganguly et al., 1988; Hofmann, 1993) should be <10% for Cl, and <30% for F and OH.

4.2.2. Annealed samples

Depth profiles were acquired for four samples that were annealed at 800–900 °C, and one sample (*DAp16*) oriented $\parallel$ ***a*** that was annealed at 950 °C (Table 1; Fig. 5). P intensities increase with increasing distances from the thin-film surface, till reaching the substrate (Fig. 5), which can be explained by P migration towards the thin film during annealing. This interference combined with that of the mixing layers produced by SIMS analysis (see above) make it difficult to precisely determine the location of the interface. Here we consider the position where the P intensity just reaches the plateau as the approximate location of the interface (±10 nm, considering the existence of mixing layers). By doing this we find that the thin films have thickness of ~120 (±10) nm (*TF4*), ~140 (±10) nm (*TF2*), and ~170 (±10) nm (*TF7*), and the profile lengths (in substrates) are ~400–800 nm for Cl, and ~100–400 nm for F and OH.

Uphill Cl diffusion was observed in two depth profiles $\parallel$ ***c***, and one profile $\parallel$ ***a*** (Fig. 5), in the crystal-powder couples (Fig. 4). In the four crystals oriented $\parallel$ ***c***, the OH profiles show larger differences between the thin film and the substrate compared to those of F and Cl, which is expected from the unannealed samples that have significantly higher OH in the thin film than in the substrate. Two samples annealed at 900 °C (*DAp11* for 0.67 hours; *DAp15* for 2 hours) show longer Cl profiles (~500 and ~650 nm, respectively) than sample *DAp9* that was annealed at 800 °C for 3.67 hours (~300 nm). Compared to the crystals oriented $\parallel$ ***c*** mentioned above, the crystal oriented $\parallel$ ***a*** (*DAp16*) that was annealed for longer durations (~21 hours) at higher temperature (950 °C) shows rather short profile lengths (e.g. ~300–400 nm for Cl).

The F profiles of *DAp11* measured with NRA and SIMS show a good match, but we noticed that F concentrations measured with NRA at same sample position decrease by as much as ~1.6 wt. % after tens of minutes bombardment of the ion beam (Supplementary Fig. S8). This can be explained by F migration while exposed under the high-energy ion beam (340–420 kV, ~200 nA). A similar phenomenon has been observed in analyses of H with the same instrument (Becker and Rogalla, 2016). Considering this, we did not use the NRA data for diffusion modelling. Nevertheless, the generally good match between F profiles acquired using the two methods, i.e., directly measured with NRA, and derived from SIMS and AFM data, validates the concentration-distance relationships converted from SIMS data, which we have used for diffusion modelling (see below).

5. Multicomponent diffusion modelling used for calculating the diffusion rates

We have found that the diffusion of Cl occurs against its own concentration gradient, i.e., namely "uphill" diffusion. Such "uphill" diffusion has been found in other multicomponent solid solutions (e.g. Ca diffusion in Ca-Fe-Mg-Mn garnet; Ganguly, 2010), and it is related to the coupling between the different components where flux of a component is affected by those of others that have similar chemical properties and occupy the same site of the crystal structure (Chakraborty and Ganguly, 1991; Ganguly, 2002). The "uphill" Cl diffusion in apatite can be explained by the coupling of Cl with F and OH (at the same anion site) and the need of mass conservation at this site (Piccoli and Candela, 2002; Hughes and Rakovan, 2015). Below we briefly describe the theory of multicomponent diffusion, and the modelling approach used for calculating diffusivities in this study.

5.1. Background of multicomponent diffusion

In an n-component system ($n \geq 3$), the diffusion of each component depends on $(n-1)$ independent components, where the

flux of the n-th component is fixed by those of the other components because of stoichiometric constraint ($\Sigma X_i = 1$). Considering one-dimensional diffusion, the diffusivity of component i can be expressed following the Fick-Onsager relation as:

$$\frac{\partial C_i}{\partial t} = \sum_{j=1}^{n-1} \frac{\partial}{\partial x}\left(D_{ij}\frac{\partial C_j}{\partial x}\right) \quad (1)$$

where D_{ij} is a diffusion coefficient that is related to the tracer diffusion coefficients of i and j, and the thermodynamic mixing properties of the solution (see Eq. (3) below). Following Ganguly (2002), the $(n-1)$ equations in the form of Eq. (1) can be written as:

$$\frac{\partial \boldsymbol{C}}{\partial t} = \frac{\partial}{\partial x}\left(\frac{\boldsymbol{D}\partial \boldsymbol{C}}{\partial x}\right) \quad (2)$$

where $\boldsymbol{C}$ is a concentration vector of $(n-1)$ independent components, and $\boldsymbol{D}$ is an $(n-1)$ by $(n-1)$ matrix (referred to as $\boldsymbol{D}$-matrix) that is comprised of D_{ij}s. Given that F^-, Cl^- and OH^- have the same charge, D_{ij} can be calculated using the formulation of Lasaga (1979):

$$D_{ij} = \left[D_i^*\delta_{ij} - \frac{X_i D_i^*}{\sum_{k=1}^{n} X_k D_k^*}\left(D_j^* - D_n^*\right)\right](TF) \quad (3)$$

where δ_{ij} is the Kronecker delta, i.e., $\delta_{ij} = 1$ when $i = j$, and $\delta_{ij} = 0$, when $i \neq j$, and X_i is the mole fraction of i, D_i^* is the tracer diffusion coefficients of i (equivalent to its diffusivity when in the absence of other components; cf. Zhang and Cherniak, 2010), and TF represents the Thermodynamic Factor of the solid solution (e.g. equal to unity for an ideal solution).

The mixing of F-Cl-OH in the Cl-rich apatite has been found to be thermodynamically non-ideal especially at low temperatures (Li and Costa, 2020), but that is not the case here given that the crystals used in our experiments are fluorapatite that contain low Cl ($X_{Cl} < 0.08$). Using the formulations for activity coefficients (γ_i^{Ap}) of Li and Costa (2020), we find rather small differences between the γ_i^{Ap}s of the core and rim of the crystals used in our experiments (at corresponding temperatures), e.g., for *DAp11* that was annealed at 900 °C, the ratios of γ_i^{Ap}s in the crystal rim to γ_i^{Ap}s in the core are close to unity (≈0.96–1.2). Considering this, the apatite investigated in this study can be treated as nearly ideal solution, i.e., $TF \approx 1$ in Eq. (3).

5.2. Simulation of the measured diffusion profiles

For diffusion modelling, we converted F-Cl-H_2O concentrations acquired with EPMA and SIMS analyses into mole fractions (cf. Li and Costa, 2020), and took initial and boundary conditions as measured from the unzoned area and the rim (or surface) of each crystal (or substrate) (Fig. 6). For the substrate-thin film samples, we only used the profiles that have fixed P intensities in the substrate (i.e., at the plateaus in Fig. 5e) for diffusion modelling, such that the interference induced by mixing layers at the interface on the calculated diffusivities were minimized (see Section 4.2).

To simultaneously fit the diffusion profiles of F, Cl and OH, we have developed a three-component diffusion model (programmed with MATLAB), following Chakraborty and Ganguly (1991). By inputting a series of estimated values of $\{D_F^*,\ D_{Cl}^*,\ D_{OH}^*\}$, the elements of the $\boldsymbol{D}$ matrix (D_{ij} in Eq. (3)) were calculated at each grid point for every time step using a finite difference algorithm. Running the algorithm for many times using different input values of D_i^*s, we found out a group of D_i^*s that are able to reproduce the profiles of the three components determined for each sample. Best fits were judged by visual inspection following Borinski et al. (2012) (Fig. 6; Supplementary Figs. S11-16). The MATLAB-based program mentioned above has been developed into a user-friendly online tool (*ApTimer*: https://aptimer.wovodat.org/) for calculating timescales of F-Cl-OH diffusion in natural apatite (see Section 6.2).

5.3. Uncertainties of the diffusivities

The maximal and minimal diffusion rates were determined by fitting the modelled profiles to the measured ones with consideration of the errors from EPMA or SIMS analysis (see Supplementary Material). Relative errors in mole fractions (X_i) of F, Cl and OH propagated from SIMS analysis are about 2–5% for X_F, 3–5% for X_{Cl}, and 9–16% for X_{OH}, and those from EPMA analysis are about 1–2% for X_F, 1–2% for X_{Cl}, and 4–20% for X_{OH}. For the single-component diffusion model used for S, relative error in $^{34}S/^{18}O$ from SIMS analysis is ~2–4%.

5.4. Calculated diffusion coefficients

The calculated diffusivities of F, Cl and OH show a general relation of $D_F^* > D_{Cl}^* > D_{OH}^*$ (all $\parallel \boldsymbol{c}$; Table 1). The D_{Cl}^* values are in general smaller than those reported by Brenan (1994), e.g., at 1100 °C, we find $D_{Cl}^* = 5\ (\pm 1) \times 10^{-16}$ m^2/s, which is ~2–8 times smaller (Fig. 7). The values of D_F^* and D_{OH}^* show larger variations than those of D_{Cl}^*. The ranges of D_F^*s determined in this study cover those in Brenan (1994), but our best-fit values of D_F^* are ~4 times smaller. The calculated tracer diffusion coefficients ($\parallel \boldsymbol{c}$) define the following Arrhenius relations:

$$D_{Cl}^* = 7\begin{pmatrix}+12\\-4\end{pmatrix} \times 10^{-5} \times \left[exp\left(\frac{-294\ (\pm 12)\ \text{kJ}\cdot\text{mol}^{-1}}{RT}\right)\right] \text{m}^2\cdot\text{s}^{-1} \quad (4)$$

$$D_F^* = 5\begin{pmatrix}+49\\-5\end{pmatrix} \times 10^{-4} \times \left[exp\left(\frac{-308\ (\pm 76)\ \text{kJ}\cdot\text{mol}^{-1}}{RT}\right)\right] \text{m}^2\cdot\text{s}^{-1} \quad (5)$$

$$D_{OH}^* = 4\begin{pmatrix}+11\\-3\end{pmatrix} \times 10^{-2} \times \left[exp\left(\frac{-401\ (\pm 39)\ \text{kJ}\cdot\text{mol}^{-1}}{RT}\right)\right] \text{m}^2\cdot\text{s}^{-1} \quad (6)$$

The activation energy (E_a) of Cl diffusion (~294 kJ·mol^{-1}; $\parallel \boldsymbol{c}$) found in this study is within the range of that determined by Brenan (1994) (~284 ± 30 kJ·mol^{-1}), whereas the pre-exponential factor (≈7.2 × 10^{-5} m^2/s) is about half of that reported by Brenan (1994). The diffusion of OH ($\parallel \boldsymbol{c}$) is much slower with a greater activation energy than those of F and Cl, and is at least one order of magnitude slower than the self-diffusion of O ($\parallel \boldsymbol{c}$) at the oxygen site of apatite (Farver and Giletti, 1989). The higher activation energy of OH^- could be related to the fact that OH^- is a diatomic anion, and its diffusion requires simultaneous transport of O and H in the apatite structure. H diffusivities were determined by Higashi et al. (2017) at 500-700 °C (Fig. 7), and extrapolation of their data to the temperatures of our experiments (800–1100 °C) implies faster H diffusion than Cl.

For diffusional anisotropy, we find that at 950 °C, D_{Cl}^* ($\parallel \boldsymbol{c}$) is ~90–400 times faster than D_{Cl}^* ($\parallel \boldsymbol{a}$), and D_{OH}^* ($\parallel \boldsymbol{c}$) is ~1–2 orders of magnitude faster than D_{OH}^* ($\parallel \boldsymbol{a}$), in agreement with the anisotropic diffusion of Cl and O found in previous studies (Farver and Giletti, 1989; Brenan, 1994) (Fig. 7). F diffusivities seem to be

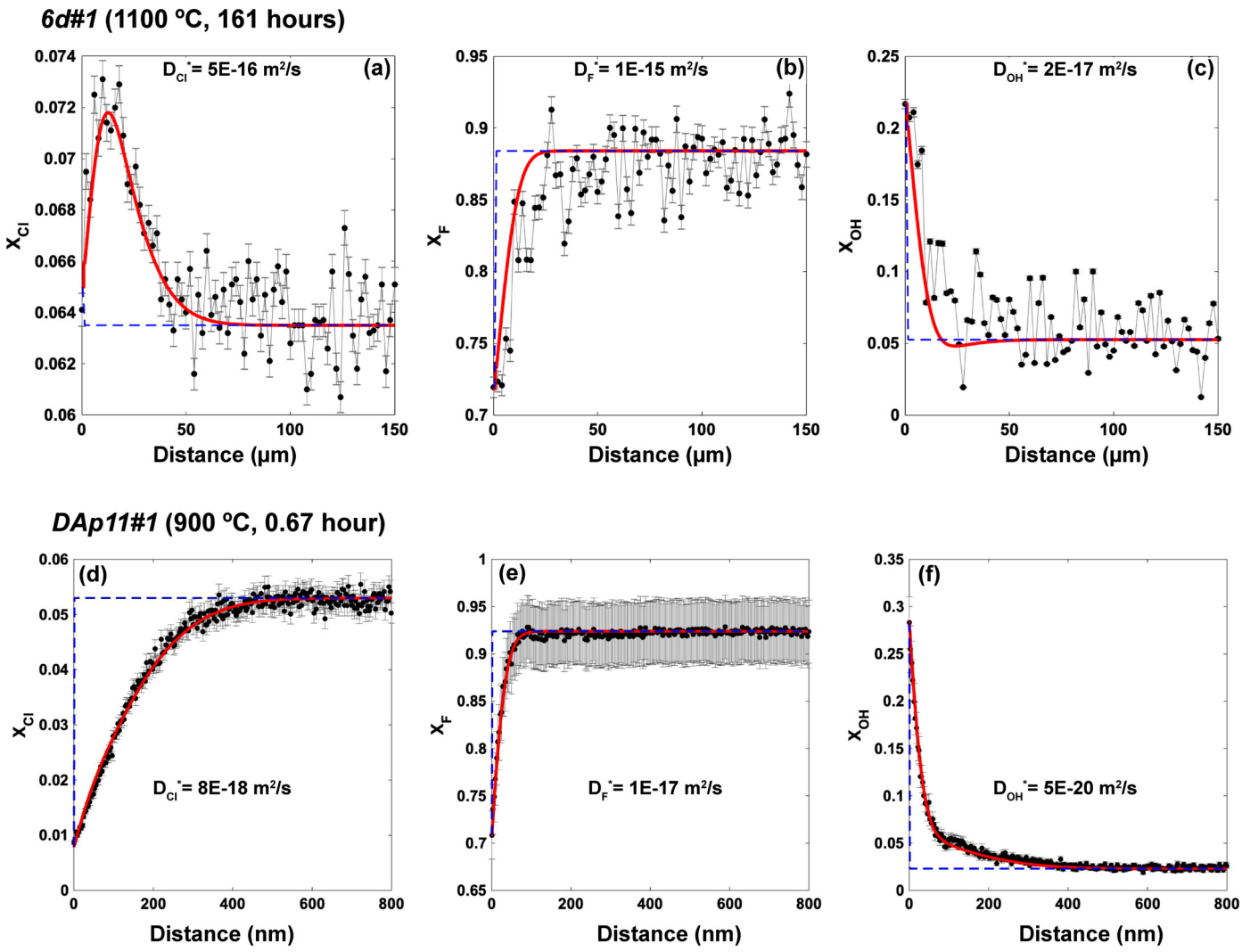

Fig. 6. Profiles of F, Cl, and OH (in mole fractions; *black dots*) measured for sample 6*d*#1 using EPMA (panels *a*-*c*) and for sample *DAp11* using SIMS (panels *d*-*f*), and their best-fit models (*red solid lines*). Initial and boundary conditions (*blue dashed lines*) were determined by the compositions at the unzoned areas and the crystal rim. Error bars show 2 s.d. of the calculated mole fractions (with analytical errors considered; see text).

also faster $\| \boldsymbol{c}$ than $\| \boldsymbol{a}$, but given large uncertainties in these values, we cannot provide good constraints on the anisotropic properties of F diffusion.

The valence states of S in apatite determined by Konecke et al. (2017) showed that the S in Durango apatite mainly occurs as S^{6+} (in the tetrahedral site), whereas the apatite crystallizing at reduced conditions (e.g. at the fayalite-magnetite-quartz redox buffer) contains predominantly S^{2-} (at the anion site). Although our experiments were performed under reduced conditions (at WM buffer), to convert the total ~1600 ppm S in these crystals from S^{6+} to S^{2-}, while keeping the charge balance, requires large amounts of additional cations, which seems unrealistic given the experimental setting. Thus, we have taken the S in our experimental crystals as S^{6+}, and used a single-component diffusion model (built on a finite-difference algorithm) to calculate S diffusivities (see model fits in Supplementary Material). We find a general relation of $D_S > D^*_{Cl} > D^*_{OH}$ (all $\| \boldsymbol{c}$), and that D_S ($\| \boldsymbol{c}$) at 800 °C ($\approx 1.2 \times 10^{-19}$ m^2/s) is about one tenth of that at ~900 °C (Table 1). Based on the two values of D_S ($\| \boldsymbol{c}$), we are not able to precisely determine the activation energy for S diffusion, but the extrapolation of these values implies that S diffusion $\| \boldsymbol{c}$ could be two orders of magnitude faster than that $\| \boldsymbol{a}$ (Fig. 7).

Compared to diffusivities of trace elements reported in literature (e.g. Pb, Sr, Mn, LREE; Watson et al., 1985; Cherniak, 2000, 2005, 2010), those of F, Cl and S ($\| \boldsymbol{c}$) determined from this study are generally greater; those of OH($\| \boldsymbol{c}$) overlap with Pb, Sr and Mn, but are greater than LREE; and that of S ($\| \boldsymbol{a}$) at 950 °C is between Mn and LREE (e.g. La) (Fig. 7). S diffusivities reported here provide a reference when investigating the formation of S zoning in natural apatite, and also the zoning of REEs if their incorporation into apatite is coupled with that of S (e.g. Pan and Fleet, 2002).

6. Discussion

6.1. Effects of apatite composition on the F-Cl-OH diffusivities

The Cl diffusivity determined in this study is generally smaller than Brenan (1994) by factors of ~2–8. This difference might be related to the diffusion sources, i.e., the sources of powders/thin films used in this study are lower in Cl and higher in OH ($X_{Cl} < 0.1$, $X_{OH} > 0.2$) than the powder-source used by Brenan (1994) ($X_{Cl} > 0.5$, $X_{OH} < 0.02$; estimated using concentrations reported in their study). This is consistent with the findings of Brenan (1994) that Cl diffusion in OH-rich crystals is slower than that in OH-poor crystals, likely because the flux of Cl is affected by that of

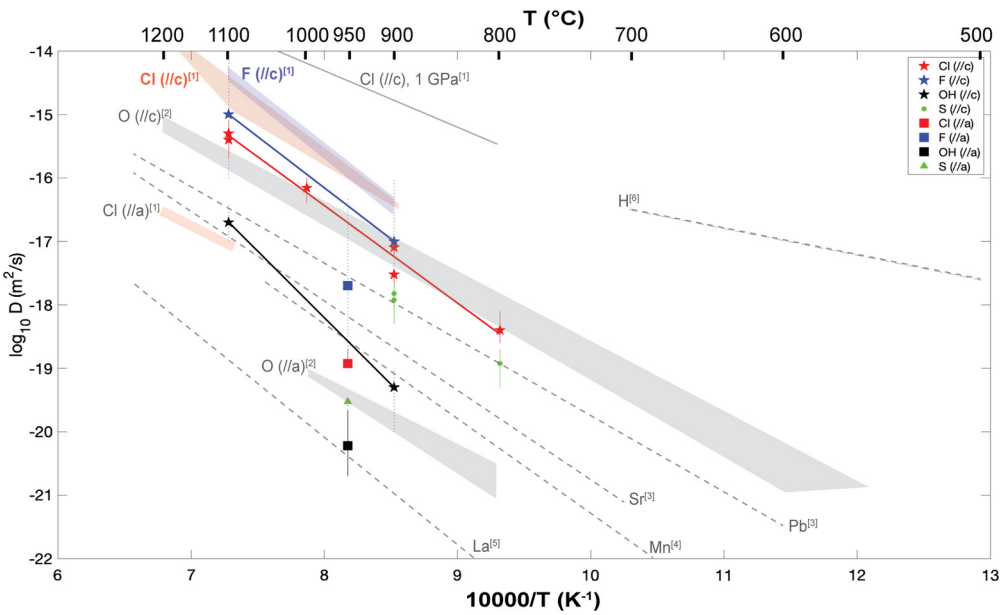

Fig. 7. Calculated diffusion coefficients of Cl, F, OH and S in this study (marked in solid symbols), compared with literature data for the diffusivities of F (1-atm), Cl (1-atm, 1 GPa), O (200 MPa), H (1-atm), and trace elements (*dotted lines*). The diffusion rates of La are shown as the representative of LREE, which were found to be of similar values. Data sources: [1] Brenan, 1994; [2] Farver and Giletti, 1989; [3] Cherniak, 2010; [4] Cherniak, 2005; [5] Cherniak, 2000; [6] Higashi et al., 2017.

OH considering the multicomponent diffusion. Considering this, to perform diffusion modelling of experimental/natural apatite that contains at least two components among F, Cl and OH, one should apply a two- or three-component diffusion model as shown below.

6.2. Application to natural volcanic apatite for determining magma ascent rates

The Arrhenius relations in Eqns. (4)–(6) can be used to calculate F, Cl, and OH diffusivities and applied to estimate diffusion timescales from natural apatite. Cl diffusion into apatite can be driven by changes in Cl-H_2O-F contents of the melt during magmas ascent (Li, 2019; also shown below), such that the timescale constrained by diffusion modelling can approximately reflect the timescale of magma ascent, and be used to estimate the ascent rates if the magma storage depth is known. With the diffusivity data and model reported above, we show two examples of our model applications to natural systems for (1) calculating the time-velocity of magma ascent by modelling diffusion profiles measured from the Cl-zoned apatite (Fig. 8), and (2) estimating the minimal velocity of magma ascent when Cl zoning is absent in apatite (Fig. 9).

6.2.1. Timescales modelled for the Cl-zoned apatite from the Merapi 2006 eruption

Apatite crystals in the groundmass of volcanic bombs from the 2006 eruption at Merapi volcano (Indonesia) share a feature of Cl-rich, F-rich and OH-poor zones over distances of 3–7 μm at their rims (Fig. 8; Li, 2019). Such zoning can be formed by (a) increase in Cl/OH and Cl/F of the melt, or (b) a higher partitioning of Cl (than F and OH) into apatite; or both. Using the model of Li and Costa (2020) for F-Cl-OH partitioning between apatite-melt, we find that a decrease in T would cause enrichment of F (rather than Cl) in apatite. Thus, we propose that the zoning in the Merapi apatite (Fig. 8) could be formed by an increase in the melt Cl/OH, predominantly caused by the combined effect of H_2O degassing and microlite crystallization which increased the melt Cl contents during the magma decompression and ascent. Thus, the time obtained from Cl diffusion in apatite can reflect the duration of magma ascent. Here we take a crystal from this deposit that has a 6-μm-wide Cl zone at its rim to illustrate how to estimate magma ascent rates.

We obtained concentration profiles (with 1-μm spacing) of F, Cl (measured using EPMA) and H_2O (calculated from stoichiometry), along a traverse that is parallel to the elongated direction of a Cl-zoned crystal (Li, 2019). These concentrations were converted into mole fractions of F, Cl and OH and modelled with the three-component diffusion approach described above. We calculated the diffusivities along the direction of the traverse ($D_i^{traverse}$, i = F, Cl, OH) using the equation below (Costa et al., 2008):

$$D_i^{traverse} = D_i^a(cos\alpha)^2 + D_i^b(cos\beta)^2 + D_i^c(cos\gamma)^2 \quad (7)$$

where D_i^a, D_i^b and D_i^c are the diffusivities of component i parallel to the $\boldsymbol{a}$-, $\boldsymbol{b}$-, $\boldsymbol{c}$-axis, and α, β, and γ are the angles between the traverse and each axis.

Based on the orientation of the crystal axes determined by EBSD, we find $\gamma \approx 18°$, and $\alpha \approx \beta \approx 72°$ (given that F-rich apatite has a hexagonal structure). The D_i^c is known from this study for T = 800–1100 °C, but the D_i^a is only known for T = 950 °C. Using the D_i^c and D_i^a determined at 950 °C and assuming $D_i^a \approx D_i^b$ (for hexagonal apatite), we find that the value of $D_i^{traverse}$ calculated from Eq. (7) is approximately equal to that calculated from an equation simplified from Eq. (7), i.e., $D_i^{traverse} \approx D_i^c \cdot (cos\gamma)^2$, with differences of only ~2–3% for F and Cl, and ~6% for OH. This is because the diffusion rates of Cl and OH are much greater $\| \boldsymbol{c}$ than $\| \boldsymbol{a}$ of apatite. Considering this, we have used $D_i^{traverse} \approx D_i^c \cdot (cos\gamma)^2$ as an approximation of Eq. (7) to calculate $D_i^{traverse}$ at 800–1100 °C.

Taking T ≈ 900 °C for the dacitic to rhyolitic groundmass melt of the Merapi 2006 eruption, the calculated diffusivities are $D_{Cl}^{traverse} \approx 5 \times 10^{-18}$ m^2/s, $D_F^{traverse} \approx 9 \times 10^{-18}$ m^2/s, and $D_{OH}^{traverse} \approx 5 \times 10^{-20}$ m^2/s. For diffusion modelling, we have taken the initial condition as a homogeneous profile with the same composition as the crystal core, and the boundary condition as the composition determined at the crystal rim. By running the diffusion model using a range of estimated time values, we obtained the best fits that correspond to times of ~300–380 hours (Fig. 8c,

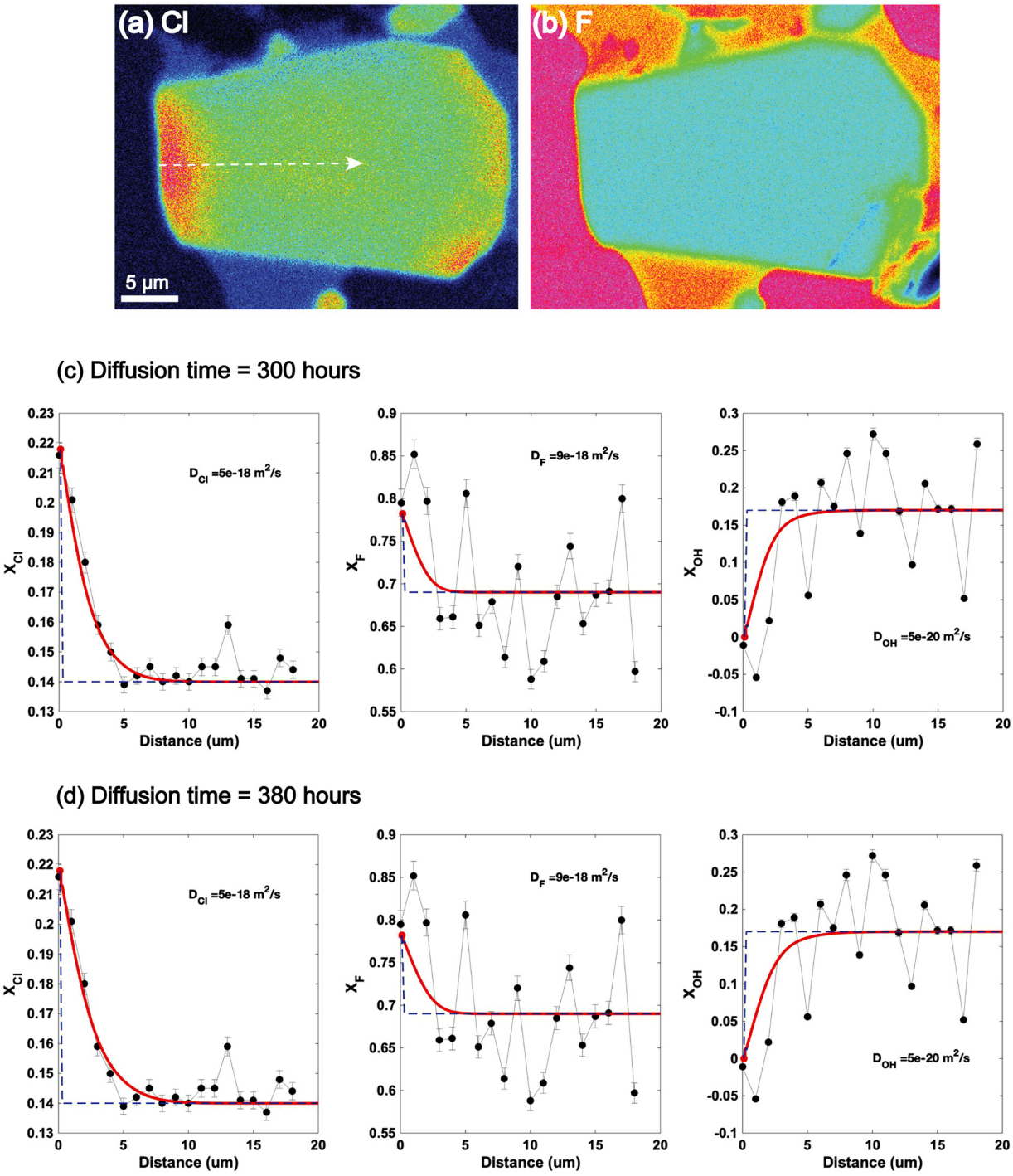

Fig. 8. X-ray maps of (a) Cl, and (b) F acquired from a groundmass apatite crystal from the Merapi 2006 eruption deposits. Concentration profiles of F, Cl, and H_2O from EPMA traverse nearly parallel to the crystal ***c***-axis (*dashed line with arrow* in panel *a*) were converted into mole fractions for diffusion modelling (*black dots* in panels *c* and *d*). *Red lines* in panels *c* and *d* show best-fit results from diffusion models with calculated timescales, i.e., 300–380 hours at 900 °C. *Blue dashed lines* show the initial and boundary conditions used for modelling. Error bars show 2 s.d. of mole fractions derived from EPMA analysis.

d), i.e., ∼12–16 days. These diffusion times overlap with the duration of ∼14–20 days between the start of volcanic unrest and the 2006 eruption, suggested by previous deformation and seismic studies (Ratdomopurbo et al., 2013; Aisyah et al., 2018).

A caveat from the model above is the assumption of a fixed boundary condition (the composition of the crystal rim), which is likely to vary according to changes in the Cl-F-OH contents of the melt, and their partitioning into apatite as mentioned above. In addition, a decrease in temperature during the ascent could lead to slower diffusion rates. Both factors need to be incorporated in future modelling efforts. Moreover, the calculation shown above can be carried out only when Cl/OH/F zoning in apatite is long enough to be measured (e.g. ≥3 μm; depending on the analytical instrument used), which is not always the case. For example, none of the apatite crystals from the Merapi 2010 deposits are zoned of Cl/OH/F, which is likely related to a much faster magma ascent for this eruption (Li, 2019). The unzoned crystals may only provide information on the maximum time as discussed below.

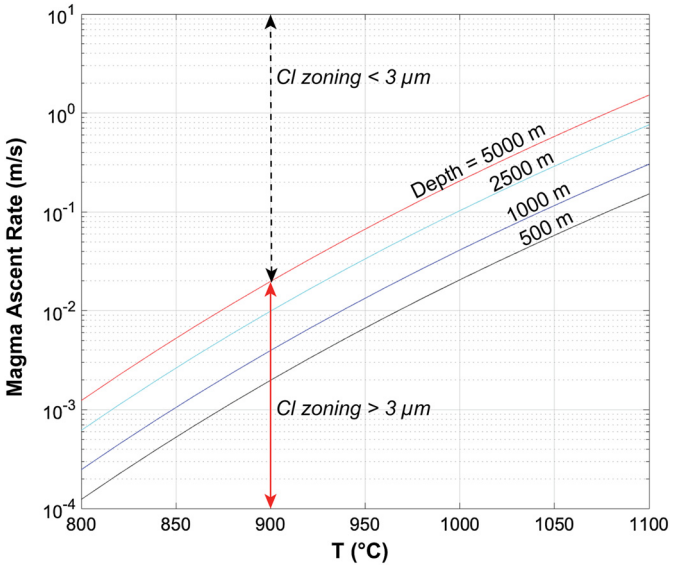

Fig. 9. Magma ascent rates calculated from timescales of Cl diffusion in groundmass apatite (assuming profile length = 3 μm) at 800-1100 °C, and varying pre-eruptive magma storage depths. 3 μm is assumed as the minimum length of Cl zoning in apatite that can be observed/analyzed by EPMA and be used for diffusion modelling (see text). For example, for a system at 900 °C, and magma storage depth of 5000 m, the groundmass apatite with Cl zoning of <3 μm would imply magma ascent rates of >0.02 m/s (marked in *black dashed line with arrows*).

6.2.2. Magma ascent rates estimated from zoning distances of Cl in volcanic apatite

We have shown that the Cl-rich rim of apatite in the Merapi 2006 deposits was formed by decompression-induced H_2O loss and the associated microlite crystallization that increased the melt Cl contents during the ascent. A faster magma ascent could lead to less time for H_2O loss from the melt and for the growth of microlites, which limit the enrichment of melt Cl, and thus the zoning mentioned above may not be formed. Thus, a lack of "obvious" Cl zoning in groundmass apatite may reflect a minimum magma ascent velocity. Here we define the "obvious" Cl zoning that can be observed/analyzed by EPMA, and be used for diffusion modelling, as being wider than 3 μm. Applying this threshold value (i.e., 3 μm) and diffusivities determined from this study to the unzoned groundmass apatite in Merapi 2010 eruption deposits, we find that the average magma ascent rate before this eruption (calculated using magma storage depth of 2.5–5 km and T of 900–925 °C) should be >0.01–0.04 m/s. Using the same pre-eruptive storage depths for the magmas erupted in 2006, we obtain ascent rates that are about an order of magnitude smaller, i.e., 0.002–0.005 m/s. Such large difference in magma ascent rates between the two eruptions agrees with the recorded one-order-of-magnitude faster extrusion rates of the 2010 explosive eruption (Pallister et al., 2013) than those of the 2006 effusive eruption (Ratdomopurbo et al., 2013).

The two examples above have shown that our diffusion model can be used to unravel the magma ascent times and rates of effusive and explosive eruptions. The two factors addressed above that relate to the formation of OH-Cl-F zoning in apatite during magma ascent, i.e., H_2O-Cl-F concentrations in the melt, and their partitioning into apatite, need to be considered when applying this model to study other volcanoes.

7. Conclusions

We report new experimental data for the diffusion rates of F, Cl and OH in apatite at 800–1100 °C and 1-atm, and first published data for the diffusivities of S. The uphill Cl diffusion we observed reflects the multicomponent diffusion of F, Cl and OH, and highlights that these anions are in the same anion column of the apatite crystallographic structure. We have used a three-component diffusion model to calculate the elemental diffusivities, and found that the tracer diffusion rates of Cl are slower than those reported in the literature that considers single-component diffusion. The new diffusion data and model have been used to develop a user-friendly online tool (*ApTimer*) for calculating timescales of F-Cl-OH diffusion in natural apatite (https://aptimer.wovodat.org/). Application of this model to the Cl-zoned apatite from the Merapi 2006 eruption deposits gives approximate timescales of ~2 weeks. We interpret this as the duration of magma ascent, and find it matching with the duration of pre-eruptive unrest observed from volcano monitoring. More accurate magma ascent times could be obtained by adding the effect of changing boundary conditions due to changes in F-Cl-OH contents of magmas during ascent, and utilizing additional experimental data at crustal pressures (e.g. 100–200 MPa). The findings from this study can be further applied to study volatile fluxing in plutonic systems, and to interpret the volatile records in apatite from the Moon and Mars.

CRediT authorship contribution statement

Weiran Li: Data curation, Formal analysis, Investigation, Methodology, Software, Writing - original draft. **Sumit Chakraborty:** Investigation, Methodology, Resources, Writing - review & editing. **Kazuhide Nagashima:** Data curation, Investigation, Writing - review & editing. **Fidel Costa:** Conceptualization, Funding acquisition, Supervision, Writing - review & editing.

Declaration of competing interest

The authors declare that they have no known competing financial interests or personal relationships that could have appeared to influence the work reported in this paper.

Acknowledgements

This work is part of the Ph.D. thesis of W. Li, who would like to thank R. Dohmen, H.-W. Becker and D. Rogalla for assistance with sample preparation and guidance in NRA (at Ruhr University Bochum), and J. Herrin and R. I. Made for support during EPMA and TEM analyses (at NTU). W. Li also thanks Y. Zhang for generously providing the apatite standards, P. Chowdhury for discussion on diffusion modelling and coding with MATLAB, and H. Pham and N. Ta for their assistance in establishing the online calculator. We are grateful to D. Cherniak and an anonymous reviewer for their constructive comments on an earlier version of this manuscript, and thank H. Handley for editorial handling. This work comprises Earth Observatory of Singapore contribution no. 324, and was funded by Dr. Stephen Riady Scholarship for Geoscience students awarded to W. Li during 2017-2018, and by a National Research Foundation Singapore Investigatorship Award (NRF-NRFI2017-06).

Appendix A. Supplementary material

Supplementary material related to this article can be found online at https://doi.org/10.1016/j.epsl.2020.116545.

References

Aisyah, N., Iguchi, M., Subandriyo, Budisantoso, A., Hotta, K., Sumarti, S., 2018. Combination of a pressure source and block movement for ground deformation analysis at Merapi volcano prior to the eruptions in 2006 and 2010. J. Volcanol. Geotherm. Res. 357, 239–253.

Baxter, E.F., 2010. Diffusion of noble gases in minerals. Rev. Mineral. Geochem. 72, 509–557.

Becker, H.W., Rogalla, D., 2016. Nuclear reaction analysis. In: Fritzsche, H., Huot, J., Fruchart, D. (Eds.), Neutron Scattering and Other Nuclear Techniques for Hydrogen in Materials. Springer, pp. 315–336.
Borinski, S.A., Hoppe, U., Chakraborty, S., Bhowmik, S.K., 2012. Multicomponent diffusion in garnets I: general theoretical considerations and experimental data for Fe–Mg systems. Contrib. Mineral. Petrol. 164, 571–586.
Boudreau, A.E., 1995. Fluid evolution in layered intrusions: evidence from the chemistry of the halogen-bearing minerals. In: Magmas, Fluids and Ore Deposits, pp. 25–46.
Boyce, J.W., Hervig, R.L., 2008. Magmatic degassing histories from apatite volatile stratigraphy. Geology 36, 63–66.
Boyce, J.W., Hervig, R.L., 2009. Apatite as a monitor of late-stage magmatic processes at Volcán Irazú, Costa Rica. Contrib. Mineral. Petrol. 157, 135–145.
Boyce, J.W., Tomlinson, S.M., McCubbin, F.M., Greenwood, J.P., Treiman, A.H., 2014. The lunar apatite paradox: supplementary materials. Science 344 (80), 400–402.
Brenan, J., 1994. Kinetics of fluorine, chlorine and hydroxyl exchange in fluorapatite. Chem. Geol. 110, 195–210.
Brounce, M., Boyce, J., McCubbin, F.M., Humphreys, J., Reppart, J., Stolper, E., Eiler, J., 2019. The oxidation state of sulfur in lunar apatite. Am. Mineral. 104, 307–312.
Chakraborty, S., Ganguly, J., 1991. Compositional zoning and cation diffusion in garnets. In: Ganguly, J. (Ed.), Diffusion, Atomic Ordering, and Mass Transport, vol. 8. Springer Verlag, pp. 120–175.
Cherniak, D.J., 2000. Rare earth element diffusion in apatite. Geochim. Cosmochim. Acta 64, 3871–3885.
Cherniak, D.J., 2005. Uranium and manganese diffusion in apatite. Chem. Geol. 219, 297–308.
Cherniak, D.J., 2010. Diffusion in accessory minerals: zircon, titanite, apatite, monazite and xenotime. Rev. Mineral. Geochem. 72, 827–869.
Cornejo, P.C., Mahood, G.A., 1997. Seeing past the effects of re-equilibration to reconstruct magmatic gradients in plutons: La Gloria Pluton, central Chilean Andes. Contrib. Mineral. Petrol. 127, 159–175.
Costa, F., Dohmen, R., Chakraborty, S., 2008. Time scales of magmatic processes from modeling the zoning patterns of crystals. In: Reviews in Mineralogy and Geochemistry, pp. 545–594.
Dohmen, R., Chakraborty, S., Becker, H.W., 2002. Si and O diffusion in olivine and implications for characterizing plastic flow in the mantle. Geophys. Res. Lett. 29, 1–4.
Farver, J.R., Giletti, B.J., 1989. Oxygen and strontium diffusion kinetics in apatite and potential applications to thermal history determinations. Geochim. Cosmochim. Acta 53, 1621–1631.
Ganguly, J., 2002. Diffusion kinetics in minerals: principles and applications to tectono-metamorphic processes. In: EMU Notes in Mineralogy, pp. 271–309.
Ganguly, J., 2010. Cation diffusion kinetics in aluminosilicate garnets and geological applications. In: Zhang, Y., Cherniak, D.J. (Eds.), Reviews in Mineralogy and Geochemistry, pp. 559–601.
Ganguly, J., Bhattacharya, R.N., Chakraborty, S., 1988. Convolution effect in the determination of compositional profiles and diffusion coefficients by microprobe step scans. Am. Mineral. 73, 901–909.
Greenwood, J.P., Itoh, S., Sakamoto, N., Vicenzi, E.P., Yurimoto, H., 2008. Hydrogen isotope evidence for loss of water from Mars through time. Geophys. Res. Lett. 35, 1–5.
Greenwood, J.P., Itoh, S., Sakamoto, N., Warren, P., Taylor, L., Yurimoto, H., 2011. Hydrogen isotope ratios in lunar rocks indicate delivery of cometary water to the Moon. Nat. Geosci. 4, 79–82.
Higashi, Y., Itoh, S., Hashiguchi, M., Sakata, S., Hirata, T., Watanabe, K., Sakaguchi, I., 2017. Hydrogen diffusion in the apatite-water system: fluorapatite parallel to the c-axis. Geochem. J. 51, 115–122.
Hofmann, S., 1993. Approaching the limits of high resolution depth profiling. Appl. Surf. Sci. 70/71, 9–19.
Hughes, J.M., Rakovan, J.F., 2015. Structurally robust, chemically diverse: apatite and apatite supergroup minerals. Elements 11, 165–170.
Ketcham, R.A., 2015. Technical note: calculation of stoichiometry from EMP data for apatite and other phases with mixing on monovalent anion sites. Am. Mineral. 100, 1620–1623.
Konecke, B.A., Fiege, A., Simon, A.C., Parat, F., Stechern, A., 2017. Co-variability of S^{6+}, S^{4+}, and S^{2-} in apatite as a function of oxidation state: implications for a new oxybarometer. Am. Mineral. 102, 548–557.
Kusebauch, C., John, T., Whitehouse, M.J., Engvik, A.K., 2015. Apatite as probe for the halogen composition of metamorphic fluids (Bamble Sector, SE Norway). Contrib. Mineral. Petrol. 170, 1–20.
Lasaga, A.C., 1979. Multicomponent exchange and diffusion in silicates. Geochim. Cosmochim. Acta 43, 455–469.
Li, W., 2019. Eruptive styles of subduction-zone volcanoes: investigation of magmatic volatile budgets and ascent rates using apatite. Doctoral thesis. Nanyang Technological University, Singapore.
Li, W., Costa, F., 2020. A thermodynamic model for F-Cl-OH partitioning between silicate melts and apatite including non-ideal mixing with application to constraining melt volatile budgets. Geochim. Cosmochim. Acta 269, 203–222.
McCubbin, F.M., Nekvasil, H., 2008. Maskelynite-hosted apatite in the Chassigny meteorite: insights into late-stage magmatic volatile evolution in martian magmas. Am. Mineral. 93, 676–684.
McCubbin, F.M., Steele, A., Hauri, E.H., Nekvasil, H., Yamashita, S., Hemley, R.J., 2010. Nominally hydrous magmatism on the Moon. Proc. Natl. Acad. Sci. 107, 11223–11228.
Pallister, J.S., Schneider, D.J., Griswold, J.P., Keeler, R.H., Burton, W.C., Noyles, C., Newhall, C.G., Ratdomopurbo, A., 2013. Merapi 2010 eruption-Chronology and extrusion rates monitored with satellite radar and used in eruption forecasting. J. Volcanol. Geotherm. Res. 261, 144–152.
Pan, Y., Fleet, M.E., 2002. Compositions of the apatite-group minerals: substitution mechanisms and controlling factors. Rev. Mineral. Geochem. 48, 13–49.
Peng, G., Luhr, J.F., McGee, J.J., 1997. Factors controlling sulfur concentrations in volcanic apatite. Am. Mineral. 82, 1210–1224.
Piccoli, P.M., Candela, P.A., 1994. Apatite in felsic rocks: a model for the estimation of initial halogen concentrations in the bishop tuff (long valley) and tuolumne intrusive suite (Sierra Nevada Batholith) magmas. Am. J. Sci. 294, 92–135.
Piccoli, P.M., Candela, P.A., 2002. Apatite in igneous systems. Rev. Mineral. Geochem. 48, 255–292.
Ratdomopurbo, A., Beauducel, F., Subandriyo, J., Agung Nandaka, I.G.M., Newhall, C.G., Suharna, Sayudi, D.S., Suparwaka, H., Sunarta, 2013. Overview of the 2006 eruption of Mt. Merapi. J. Volcanol. Geotherm. Res. 261, 87–97.
Scott, J.A.J., Humphreys, M.C.S., Mather, T.A., Pyle, D.M., Stock, M.J., 2015. Insights into the behaviour of S, F, and Cl at Santiaguito Volcano, Guatemala, from apatite and glass. Lithos 232, 375–394.
Stock, M.J., Humphreys, M.C.S., Smith, V.C., Isaia, R., Brooker, R.A., Pyle, D.M., 2018. Tracking volatile behaviour in sub-volcanic plumbing systems using apatite and glass: insights into pre-eruptive processes at Campi Flegrei, Italy. J. Petrol., 1–29.
Stock, M.J., Humphreys, M.C.S., Smith, V.C., Johnson, R.D., Pyle, D.M., 2015. New constraints on electron-beam induced halogen migration in apatite. Am. Mineral. 100, 281–293.
Stormer, J., Pierson, M.L., Tacker, R.C., 1993. Variation of F and Cl X-ray intensity due to anisotropic diffusion in apatite. Am. Mineral. 78, 641–648.
Ustunisik, G., Nekvasil, H., Lindsley, D.H., Mccubbin, F.M., 2015. Degassing pathways of Cl-, F-, H-, and S-bearing magmas near the lunar surface: implications for the composition and Cl isotopic values of lunar apatite. Am. Mineral. 100, 1717–1727.
Van Hoose, A.E., Streck, M.J., Pallister, J.S., Walle, M., 2013. Sulfur evolution of the 1991 Pinatubo magmas based on apatite. J. Volcanol. Geotherm. Res. 257, 72–89.
Wang, Y., Hsu, W., Guan, Y., 2019. An extremely heavy chlorine reservoir in the Moon: insights from the apatite in lunar meteorites. Sci. Rep. 9, 1–8.
Watson, E.B., Harrison, T.M., Ryerson, F.J., 1985. Diffusion of Sm, Sr, and Pb in fluorapatite. Geochim. Cosmochim. Acta 49, 1813–1823.
Webster, J.D., Piccoli, P.M., 2015. Magmatic apatite: a powerful, yet deceptive, mineral. Elements 11, 177–182.
Zhang, Y., Cherniak, D.J., 2010. Diffusion in minerals and melts: introduction. In: Reviews in Mineralogy and Geochemistry, pp. 1–4.